Article:
Hu, Z, Gao, H, Ramisetti, S orcid.org/0000-0002-2927-5257 et al. (4 more authors) (2019) Carbon Quantum Dots with Tracer-like Breakthrough Ability for Reservoir Characterisation. Science of the Total Environment, 669. pp. 579-589. ISSN 0048-9697

https://doi.org/10.1016/j.scitotenv.2019.03.007

Carbon Quantum Dots with Tracer-like Breakthrough Ability for Reservoir Characterisation

Zhongliang Hu,[a,†] *Hui Gao,*[b,c,†] *Srinivasa Ramisetti,*[a] *Jin Zhao,*[a] *Ehsan Nourafkan,*[a] *Paul W. J. Glover,*[d] *Dongsheng Wen,*[*,b,a]

[a] *School of Chemical and Process Engineering, University of Leeds, Leeds, LS2 9JT, UK*

[b] *School of Aeronautic Science and Engineering, Beihang University, Beijing, 100191, China*

[c] *Ming Wai Lau Centre for Reparative Medicine, Karolinska Institutet, Solna, 171 77, Sweden*

[d] *School of Earth and Environmental Science, University of Leeds, Leeds, LS2 9JT, UK*

* *Correspondence to: Dongsheng Wen, d.wen@leeds.ac.uk & d.wen@buaa.edu.cn*

Tel: +44(0)113 343 1299

ABSTRACT

Predictions have shown that our demand for oil and gas will continue to grow in the next decade, and future supply will become more reliant on tertiary recovery and from nonconventional resources. However, current reservoir characterization methodologies, such as well logs, cross-well electromagnetic imaging and seismic methods, have their individual limitations on detection range and resolution. Here we propose a pioneering way to use carbon quantum dots (CQDs) as nanoparticle tracers, which can be transported through a reservoir functioning as conventional tracers, while acting as sensors to obtain useful information. These hydrothermally produced CQDs from Xylose possess excellent stability in high ionic strength solutions, durable absorbance and fluorescence ability due to multi high-polarity functional group on their surfaces. Consistency between our on-line ultraviolet–visible (UV-Vis) spectroscopy and off-line Confocal laser scanning microscopy (CLSM) measurements confirms that CQDs have the tracer-like migration capability in glass beads-packed columns and sandstone cores, regardless of particle concentration and ionic strength. However, their migration ability are undermined in the column packed with crushed calcite grains with positive charge. We also demonstrate that quantitative oil saturation detection in unknown sandstone core samples can be achieved by such CQDs based on its breakthrough properties influenced by the presence of oil phase.

Keywords: Quantum dots, transport behaviour, high salinity, subsurface reservoir characterization, scalable nanotracer

1. INTRODUCTION

The overriding problem for successful water flooding or subsequent tertiary exploration of crude oil is related to the probing and mapping of subsurface reservoirs that cannot be accessed easily. Ultimately, all the information we have about a reservoir is used to build a digital model that can be solved for fluid flow. This reservoir modelling and flow simulation is extremely powerful in modern hydrocarbon exploration and production because it allows for different scenarios to be tested in order to optimise production and minimise production risk . However, many information put into the reservoir model are based on assumptions, covering a wide range from outcrop analogue data to seismic data, wireline data, routine and special core analysis data, well pressure, fluid data and so on.

Running probes in boreholes is the most common conventional method to acquire information from the reservoir, but the information they provide is insufficient because it is highly localized to the surroundings of a single borehole (Yu 2012). Images obtained using 3D and 4D seismic techniques, on the other hand, can map the totality of the reservoir (Dickens et al. 1997), which is however limited by a low resolution about 30 m vertically and laterally. In addition, the seismic method is sensitive to interfaces between layers of rock, making it difficult to for measuring the properties of a given rock layer even if that layer is substantially thicker than 30 m.

Techniques using natural tracers and isotopes, as well as various artificial tracers, are now being used to obtain the subsurface information, including fluid flow and well continuity, and are being used to upgrade reservoir models. Most of these tracers, can only provide information about the flow connectivity (i.e., the connection between where the tracer was injected and where it came out, without any information about its pathway in between. The combination of a partitioning tracer and a conservative tracer could be used to estimate non-aqueous-phase liquid (NAPL) in porous media (Jones and Smith 2005, Brusseau et al. 2010), but this approach

suffers from limitations, especially the instability of tracers inside the harsh reservoir environment, where non-neutral pHs, high temperatures and abundant micro-biotic activity conspire to degrade the tracer and consequently affect the measurements (Sabir et al. 2000). Some dye and radioactive chemical tracers can be helpful locally but generally do not reveal the actual pathway that is taken by the host fluid from the entry well to the detection well (Hwang et al. 2012).

Recently, the injection of nanoparticles (NPs) has been proposed as a potential means for enhanced oil recovery (Luo et al. 2016, Hu et al. 2016, Hu et al. 2017) and understanding of oil displacement mechanism (Wasan and Nikolov 2003, Kondiparty et al. 2011). Encompassing the merits of DNA-tracers, the intrinsic information-coding capacity (particle type, shape, coating, etc.) could allow discrimination between two or more particle tracers coming from different sources or released at different times. Well-mobilized particles can also be used as carriers to transport an active cargo, which can record the variation of subsurface environment, or be released to the NAPL to improve its recovery. There is another potential for using NPs as reservoir sensors via special functionalization, which is responsive to reservoir temperature (Stuart et al. 2010, Alaskar 2013), special chemicals (e.g., H_2S (Hwang et al. 2014), oil (Hwang et al. 2012, Berlin et al. 2011)), or selective to rock porosity and permeability (Alaskar 2013), or responsive to external stimuli (ultrasound (Gao et al. 2015), ultra-violet light (Gao et al. 2016a, Gao et al. 2016b) and magnetic fields (Huh et al. 2011)).

All the applications reviewed above require nanoparticles have the capability to flow through a long distance, ideally like tracer, in the reservoir. However, until now, there is no nanoparticle been reported which has a tracer-like transport behaviour in the harsh reservoir environment, where temperatures and fluid salinities are high, the flow paths are highly tortuous and there is a huge surface area where the nanoparticles can be adsorbed (Yu et al. 2015). In addition, there are only few studies investigating the migration behaviour of

luminescent nanoparticle in porous media (Wang et al. 2014, Kini et al. 2014), but none of them used luminescent particles for reservoir characterization. In the present study, we propose an innovative way to use carbon quantum dots (CQDs) as nanoparticle tracers, which can be transported through a reservoir functioning as conventional tracers, while acting as sensors to obtain useful information.

In this work CQDs were synthesised by an environmental friendly scalable hydrothermal method using xylose as the precursor, which is a reliable, non-toxic and low-cost resource. The CQDs were well characterized in terms of morphology, functional groups and stability in API brine. Their transport and retention properties were also studied in the artificial column packed with glass beads at various CQD concentrations, ionic strengths, temperatures and substrates, and a tracer-like breakthrough capability was stablished. Their application as innovative oil saturation sensors was confirmed in a pilot study using core-flooding of a sandstone core plug. We believe that this combination of capabilities makes CQDs attractive for oil reservoir characterization, allowing us better understanding the reservoir.

2. MATERIALS AND METHODS

2.1 CQDs synthesis, characterizations and stability

2.1.1 Synthesis of CQDs

First, 0.2 g of D-(+)-Xylose ($C_5H_{10}O_5$) purchased from Sigma Aldrich was dissolved in 20 mL of deionised water; the solution was then transferred into a Teflon-lined, stainless steel autoclave. After being heated at 200 °C for 6 h and then cooled to room temperature, the obtained solution was centrifuged at 10000 r/min for 30 minutes to precipitate the solid black carbon particles. The supernatant, which contained fluorescent CQDs was then filtered using standard syringe filters (25 mm i.d., Fisher Scientific) with the pore size of 0.2 µm. The obtained solution was then characterized and used in the column transport tests carried out in this work.

2.1.2 CQD characterizations

A JEOL JEM-2010 transmission electron microscope (TEM) operating at 200 kV was used to characterize the morphology of CQDs. From the obtained high-resolution TEM images, CQD size was measured and analysed using Image-J software. The UV-Vis absorption spectra of CQDs were measured by a UV spectrophotometer (UV 1800, Shimadzu). The fluorescence spectra of CQDs were recorded by using the fluorescence spectrometer (LS 55, Perkin Elmer) performed with a slit width of 10 nm both for excitation and emission. The excitation wavelength was increased from 300 nm to 460 nm with a 20 nm increment. An infrared spectrometer (FTIR spectrometer 100, Perkin Elmer) was used to measure the FTIR spectra of the freeze-dried CQDs, collecting data at a spectral resolution of 4 cm^{-1}. The Raman spectra were recorded using a Raman spectrometer at an excitation wavelength of 633 nm. The hydrodynamic particle size distribution and zeta potential of CQDs in both deionised water and brine with various salinities were analysed via a Zetasizer (Zetasizer Nano ZS, Malvern Instruments Ltd), as shown in table S2 (Support Information).

2.1.3 Stability of CQDs against high salinity

The stability of CQD suspended in American Petroleum Institute (API) standard brine (8 wt% NaCl and 2 wt% $CaCl_2$) was first determined by the absorbance variation against time, measured by a UV-Vis spectrophotometer operating at a fixed wavelength of 278 nm where the absorbance peak appears. Stability was also checked by exposing the same sample under the excitation light for 220 minutes, which was long enough for the injection experiment, and the fluorescence intensity was recorded against time.

The stability of several CQDs suspensions against high salinity was also characterized by recording the transmission of near-infrared (NIR) light passing through the sample, which was centrifuged by a LUMiSizer analytical photocentrifuge (LUMiSizer 6110, Lum GmbH, Berlin, Germany). The suspension (0.5 ml) was filled in a polyamide cell with 2 mm of path length,

and then centrifuged for about 47 min at 2800 rpm (light factor of 1, 40 ^{o}C, 865 nm NIR), which is equivalent to 32 days in real time. The instability index and sedimentation velocity of CQDs was calculated by the installed software (SEPView 9.0; LUM), through the function module of 'stability analysis' and 'front tracking analysis', respectively. It is worthy to note that under NIR, there is no error added to the detected light transmission caused by excited emission from quantum dots, because the fluorescence intensity is negligible when the excitation wavelength is above 460 nm (Fig 1b).

2.2 Packed column experiments

2.2.1 Packed column experimental setup

A schematic diagram of the experiment setup is shown in the Figure 1. The column apparatus consist of a HPLC pump (Series I, Scientific Systems, Inc.) equipped with pulse damper to minimize pulsation for the benefit of downstream instrumentation, a syringe pump (KDS-410-CE, kdScientific) installed with a 100 ml syringe (32.57 mm i.d.), UV-spectrophotometer (UV 1800, Shimadzu), a borosilicate glass columns (10 cm L × 2.44 cm i.d., Glass solutions, Blacktrace Holding Ltd.), differential pressure transducer (150psi, Omega) and a by-pass route to remove the bubble left in system.

2.2.2 Preparation of packed column

Prior to use, the glass beads (Sigma Aldrich) with 30-40 mesh size fraction (425-600 μm) were thoroughly cleaned using a sequential acid wash, de-ionized water rinse, and oven-drying according to reference (Wang et al. 2010). The limestone, kindly provided by the School of Earth and Environment, University of Leeds, was crushed and sieved into 425-600 μm. In order to pack the column with constant permeability and porosity, a progression of increasingly rigorous procedures was utilized. Firstly, the dried glass beads was saturated in de-ionized water, and then deposited into glass column in 1.5 cm increments with 0.5~1 cm thick of water on the top of glass beads. After adding each layer of 1.5 cm glass beads, vibration was applied

for 3 min using a vortex mixer (Scientific Fisher). During vibration, proper strength was applied on the top of the column by one hand to keep it vertical and prevent particle from bouncing. The packing length in column was 7-7.1 cm due to the addition of O-ring blocker at both ends. To prevent glass beads from flowing out of column, the inlet and outlet blocker were fitted with 3 layers filter paper (Whatman, Grade 2). The absolute water permeability for glass beads was measured as 97 ± 10 mD based on Darcy's law. The porosity or volumetric water content (θ_w) was determined by extracting the glass beads saturated with tape water from column, and then drying them in a oven to get the mass and volume of the pore water. Due to the strict packing procedure, a constant pore volume of 12.8 ± 0.18 mL and corresponding porosity of 38.02% were obtained for different packings.

2.2.3 Transport properties in saturated column

A total of nine experiments were conducted in pre-saturated packed glass columns to evaluate the transport and retention properties of CQDs. Saline water containing $CaCl_2$ at different concentration was introduced into the column by piston pump in an up-flow mode at a Darcy velocity of 11.2 m/day, for at least 20 pore volumes (PV). Before injection into the column, the pH of this saline water was adjusted to 7 ± 0.5 by adding aliquots of either HCl or NaOH solution (1 M and 0.1 M were available). After saturating the column with saline water, 3 PV of nanoparticle suspension was introduced into the column by using a syringe pump at flow rate of 0.5 mL/min, followed by the injection of 3 PV of CQD-free brine at the same flow rate as post-flood washing process. The flow rate corresponds to a pore-water velocity of 2.56 m/d, representing a column residence time of 0.25 h. The Reynolds number (Re) was equal to 0.0186, which is several orders-of-magnitude below the limit of laminar flow in packed beds (Re<10).

The column outlet was connected to a flow cell inserted into UV-Vis spectrophotometer operating at wavelength of 310 nm, by which the effluent particle concentration was monitored

real-time. After each transport experiment, the glass beads packed in column was dissected into seven increments with 1 cm thickness, and the retained CQDs were extracted by addition of 10 grams of deionised water, followed by ultrasonication for 20 min (Fisher Scientific Ltd.). Experimental conditions for the nine column studies are summarized in Table 1.

2.2.4 Concentration determination based on fluorescence intensity

CQDs samples were collected every 3 mins after the effluent fluids flowing past the UV-Vis spectrophotometer. Then, the fluorescent intensity of collected samples were analysized by fluorescence spectrometer and their concentrations were determined by comparing the FL intensity with influent samples' FL intensity. The fluorescence intensity was measured under excitation of 360 nm UV light, and fluorescence intensity for each sample was defined as the weighted arithmetic mean value from 442 nm to 452 nm.

The packed glass beads were quantitatively extracted from the column after flooding experiments, by dissecting the packed materials into seven increments with 1 cm thickness. CLSM images of extracted glass beads were captured with a Leica TS confocal scanning system (Leica, Germany) equipped with a $63\times/1.4$ oil immersion objective. Then, the information of CQDs distribution on solid surface can be acquired from CLSM images.

2.3 Oil saturation detection in the sandstone core

2.3.1 Flooding procedure for oil detection

It is well known that it is hard to further reduce the residual oil saturation (S_{or}) after brine breakthrough in the secondary water-flooding processes in the sandstone reservoir. This suggests that oil saturation can be controlled under the value of residual oil saturation (S_{or}) in the process of brine-flooding. Before injecting CQDs suspension, brine was injected at a higher flow rate, in case the oil would be displaced out and the oil saturation was changed during the process of injecting CQDs dispersion. Another experiment setup was built up to load the Berea sandstone core (Cleveland Quarries), as shown in Figure S1 (Support Information), and the

schematic diagram in Figure S2. The experiment procedures are conducted as below, and the experiment conditions are listed in Table S2 (Support Information).

- Saturation of the core with brine (0.1 M NaCl)
- Injection of a pre-determined volume of oil into core;
- Flooding the core with brine at a high flow rate of 1 mL/min for 2 PV to simulate the secondary flooding procedure, and collection of the oil recovered during this process to determine the oil saturation after flooding.
- Injection of CQD dispersion into the core at a lower flow rate of 0.5 mL/h, and collection of the effluent sample every 3 min. Analysis of the effluent CQDs fluid samples to determine the concentration of those samples, and to generate the breakthrough curves.
- The oil saturation is then obtained from best-fit measured by the least-square error between modelled and experiment concentration profiles.

2.3.2 Simulation of CQDs transport in the sandstone core saturated with oil

To confirm the CQD transport behaviour affected by the oil presence in the sandstone rock, its transport behaviour in a Berea sandstone core was simulated by using the modified 1-D advection-dispersion-reaction (ADR) equation.

$$\frac{\partial C}{\partial t} + \frac{\rho_b}{\varepsilon}\frac{\partial S}{\partial t} = D_H \frac{\partial^2 C}{\partial x^2} - v_p \frac{\partial C}{\partial x} \quad (1)$$

Where, C is the concentration of nanoparticle in solution, S is the concentration of nanoparticles attached to the solid phase, t is the injection time, x is the distance parallel to flow direction, ρ_b is the solid bulk density, D_H is the hydrodynamic dispersion coefficient, ε is the porosity of solid phase and v_p is the velocity of the pore fluid.

In equation (1), ε is the porosity of solid phase. However, as the presence of oil phase, the transport of CQDs is confined in the aqueous phase due to their hydrophilic nature, leading to

an equivalent effect of reduced porosity, $\varepsilon' = \varepsilon - S_{or}$, where the S_{or} is the residual oil saturation in sandstone core.

The BTCs of the non-reactive tracer were fitted with the one-dimensional steady-state advection–dispersion equation. The hydrodynamic dispersion coefficient of each column was first obtained by fitting the experimental BTCs of the tracer using the CXTFIT-Excel code developed by Tang et al. (Tang et al. 2010).

3. RESULT AND DISCUSSION

3.1 Characterization of CQDs

Carbon Quantum Dots (CQDs) were facilely prepared by one-step hydrothermal carbonization of D-(+)-Xylose, an abundant and renewable precursor available in most biomass and agricultural waste materials, as shown in Figure 2a. The obtained CQDs were first characterized by UV-Vis spectrometer and fluorescence spectroscopy to check their absorbance spectra over various light wavelengths together with their luminescent properties. Figure 2b shows that the CQDs demonstrated a strong absorption in the UV region between 200 and 350 nm, with two obvious peaks at 228nm and 278 nm, which corresponds to the $\pi-\pi^*$ transitions associated with C=C bonds, and $n-\pi^*$ transitions related to hydroxyl groups, respectively (Yang et al. 2014). The fluorescence (FL) spectra shows clearly the excitation-dependent emission behaviour of the CQDs, where the fluorescent emission peaks shifted to higher wavelengths when the excitation wavelength was increased from 300 nm to 460 nm. The maximum emission intensity was obtained with an excitation at 360 nm. It shall be noted that all the emission peaks were centred in the visible spectrum region of 450-550 nm.

The transmission electron microscopy (TEM) image of the CQDs are given in Figure 2c. The black dots were clearly observed, indicating the appearance of well-dispersed CQDs with an average particle size of approximately 5 nm. The high-resolution TEM images further show

that the CQDs exhibited identical lattice fringes with a spacing of 0.24 nm, indicating their graphitic crystalline structure.

3.2 Stability of CQDs against high salinity

As shown in figure 3a, the decrease of UV absorbance was less than 4% and the normalized fluorescence intensity only saw a slightly reduction to 0.99, which verified that the CQD suspension can be stable long enough during the process of injection. In order to determine the lower limit of CQD concentration which can be detected by the UV method, samples with a set of standard concentrations were prepared by diluting an original sample of 5 ppm with API brine, and their absorbance values were measured at a fixed wavelength of 278 nm. The result indicates that the absorbance is a linear function of CQD concentration in the range of 5 ppm to as low as 50 ppb (Figure S3 in Support Information).

Stability analysis by LUMiSizer analytical photocentrifuge was conducted for four types of samples: fresh synthesised CQDs, CQDs re-dispersed in de-ionized water, CQDs re-dispersed in API brine, and CQD sample collected from one of the flooding experiments. The results in Figure 3b to Figure 3d show that all the samples examined are stable and have low instability indexs. Correspondingly, the transmission curves provided in Figure S4 in Support Information show negligible change against time for all of the samples. In Figure 3b, the CQDs dispersed in API brine only exhibited a small increase in the instability index after being centrifuged for 47 minutes at rotation speed of 2800 rpm, which is equivalent to 32 days in real time. The instability index of original CQDs after synthesis is also small but still inconsiderably higher than that in API brine. This means that, compared to the stability index of CQDs dispersed in de-ionized water which has the second highest instability index (Figure 3c) and the highest sedimentation velocity (figure 3d), the ions (Na^+ and Ca^{2+}) actually facilitated the stability of CQDs dispersed in API brine and gave rise to the lowest instability index and sedimentation velocity. Flowing pass the packed porous media slightly increased

the instability index of CQDs, but it still maintained a good stability as shown by a low sedimentation velocity in Figure 3d.

Raman spectra of the CQDs (Figure 4a) revealed a D band at 1353 cm^{-1} and a G band at 1585 cm^{-1}, which further confirmed the graphitic structures of the CDs (Ding et al. 2016). The Fourier transform infrared (FTIR) spectrum in Figure 4b reveals that there were abundant hydrophilic groups including O−H (3600-3100 cm^{-1}, 1191 cm^{-1}) and C−O (1080 cm^{-1}) on the surfaces of CQDs, thereby facilitating a good solubility in water. In addition, the O−H vibration band at ~ 3350 cm^{-1} was broad and integrated, which indicates multiple structures of hydroxyl groups on the CQD surfaces and consequently results in a high polarity and hydrophilicity (Ding et al. 2016). Those functional groups, like many research has demonstrated , also enable the carbon dots to be scalable and surface-tunarable for multi purpose application (Hwang et al. 2012, Hwang et al. 2014).

3.3 CQDs transport properties in packed columns

Two breakthrough curves (BTCs) for CQDs transport through brine-saturated (1.0 mM $CaCl_2$) columns packed with glass beads are shown in Figure 5 a&b. More than two-fold increase (i.e. from 10.6 to 24.7 ppm) in the concentration of CQDs suspensions with 1.0 mM $CaCl_2$ as electrolyte background were injected to the glass beads packed porous matrixes, i.e. the exp. G1 and G2 in Table 1 and Table 2. The resulting BTCs were almost symmetrical for both concentrations, increasing quickly to a maximum value during the injection process, followed by a rapid decline to a relative concentration (C/C_0) approaching zero during the post-flooding process. This behaviour reveals a tracer-like BTC characteristics, with the CQDs accessing all of the pore space in the glass bead column quickly when injected, and being completely removed from the glass bead pack when washed out of the column. Such behaviour differs clearly from the breakthrough performance of conventional nanoparticles, where particle retention and agglomeration were inevitable with the presence of electrolytes, as

reported in relevant research (Wang et al. 2008, Wang et al. 2012, Skaug et al. 2015), requiring an extremely long timescale for uniform nanoparticle distribution to occur and producing a retention of over 40 % even after 4 PV of particle-free brine and de-ionized water flushing (Becker et al. 2015). In this research, C/C_0 achieved 95% access after 1.6 pore volumes (PV) of injection, and nearly 100% after 2 PV, regardless of the big difference on concentrations. Once injecting CQD-free brine as the process of post flushing, the effluent particle concentration appeared as 100% from 3 to 4 PV (Figure 5a). Sharp reductions on C/C_0 were observed between 4 PV and 5 PV and the C/C_0 values in the distal portion of the BTCs are nearly zero, indicating that only small amount of CQDs retained in the column. The retention profile in Figure 5b and mass balance in Table 2 confirms that only 2.8% and 2.6% of particles were retained in the column after 3 PV brine flushing, for CQD concentrations of 10.6 ppm and 24.7 ppm, respectively.

It has been shown by a number of studies that the presence of salt can affect significantly the transport behaviour of nanoparticles greatly (Hwang et al. 2012). Consequently, we considered it is important to examine the transport effectiveness of CQDs suspended in solutions with ionic strength ranging from 1 mM to 200 mM $CaCl_2$, and to API standard brine containing 1.6 M NaCl and 0.2 M $CaCl_2$ (Bagaria et al. 2013), i.e. the exp. G1 and G3-G6 in the Table 1 and Table 2. In these experiments the concentration of CQDs was fixed at 10.05±1.23 ppm. For all ionic strengths, CQDs appeared at the outlet of the column after 1 PV injection, followed by rapid increase which levelled off to the plateau concentration at ca. 1.5 PV. Varying the ionic strength over the whole experimental range did not result in a discernible change in the shape of BTCs, as shown in Figure 5c. The CQDs showed tracer-like breakthrough behaviour and a short tailing effect for postflooding regardless of the ionic strength. The retention profiles in Figure 5d and mass balance in Table 2 show that, the retented CQDs was very low, only 0.1% to 3.7% of CQDs was retained in the glass column for all ionic

strengths, after flushed by CQD-free saline water, which is consistent with the rapid tailing behaviour recognised in brine flushing in Figure 5c.

As temperature was increased to 60 ^{o}C, the BTCs for CQDs still had a tracer-like behaviour, but experienced some fluctuations especially for 80 ^{o}C . It is also interesting to see that, as the temperature increasing, the particle broke through later and the BTCs are shift towards right as shown in Figure 5e. The retention rate was also increased as temperature rising because the maxium C/C_0 did not reach 100% after 2 PV.

Using calcite as replacement for glass bead could produce a discernible change in the shape of BTCs (Figure 5f). The CQD breakthrough for calcite column occurred at about 1 PV, which is the same as the glass bead-packed columns. However, the maximum C/C_0 was only 64.4% and achieved after around 3 PV, which is much lower and delayed, compared to 100% and 1.5 PV for the glass bead-packed columns. These observations indicate that calcite possesses a greater capacity to retain CQDs compared to glass beads. Mass balance calculations in Table 2 shows that 37.8 % of CQDs was retained in the calcite column after the injection of particle-free solution, which is consistent with the long tail shown in Figure 5f, and results from the CQDs binding to the surface of the calcite grains. This binding behaviour caused a significant change in the colour of the calcite carbonate rocks, which can be clearly observed in the inset of Figure 5f, as well as the high affinity of CQDs on the surface of calicite rock grain in Figure 6e. The reason may be attributed to the positive surface charge of calcite carbonate rock which is converse to the surface charge of CQDs in the salinity water. The carbon dots is consequently attached the grain surface due to the electrostatic force.

3.4 Coupling of absorbance and fluorescence methods

Ultraviolet and visible (UV-Vis) spectrometry has been used widely for the past 35 years, but has a number of disadvantages including, (i) cannot discriminate between the sample of interest and contaminants that absorb the same wavelength, (ii) suffers from erroneous

readings caused by the stray light reflected by suspended impurities; and (iii) there are inaccuracies caused by the influence of temperature, pH, impurities and contaminants. However, fluorescence method has some distinct advantages over absorbance method, particularly in that the sensitivity of fluorescence detection is much higher, by a factor of approximately 1000, and the influence of non-fluorescent impurities is eliminated as only molecules that fluoresce are detected,. In addition, it remains accurate over a range of up to six orders of concentration without sample dilution or modification of the sample. A coupled absorption and fluorescence method is used in this work to determine the CQD concentration.

Eleven effluent samples were collected for both the injection and the post-injection processes, from two experiments at ionic strengths of 10 mM $CaCl_2$ and API brine (exp. G3 and G6 in the Table 1). The fluorescence intensity was measured under excitation of 360 nm UV light, and fluorescence intensity for each sample was defined as the weighted arithmetic mean value from 442 nm to 452 nm. The BTCs obtained from these off-line fluorescence intensity measurements agrees well with those acquired from on-line UV determination, as shown in Figure 6 (a & b). The luminescent BTCs even delineate the tailing effect in Figure 6a at an ionic strength of API brine, which was not detected by a UV spectrometer. It should be mentioned that the determination of fluorescence intensity was conducted after 2 weeks of storage, but the fluorescence intensity remained strong enough to clarify the low concentration, regardless the CQDs was soaking in high salinity water.

The CLSM images of extracted glass beads from the packed column show a situation that CQDs were distributed homogeneously throughout the aqueous phase, and only a small number stick on the surface of glass beads (Figure 6c). After washing with de-ionized water, no luminescent particle were observed, as shown by the dark CLSM image (Figure 6d). By contrast, for the experiments using crushed limestone, CLSM shows particles adsorbed to the surfaces of the carbonate chips even after washing four times with API brine (Figure 6e), which

is consistent with the observed irreversible retention of CQDs in limestone compared to the lack of retention for the glass beads. Such irreversible adsorption phenomenon is induced by the electrostatic forces between the negatively charged CQDs and positively charged rocks.

3.5 Oil saturation detection in sandstone cores

The transport experiments above clearly show that, the CQDs are good candidates for long distance into sandstone reservoir. The particular properties which make them a good choice are (i) their stability in high ionic strength media, (ii) mobility allowing both full saturation and transport from the porous medium, (iii) low adsorbance to quartz, and (iv) their easy-detected photoluminescent properties. Consequently we propose that CQDs may be used as innovative hydrocarbon sensors for the detection of the oil saturation in sandstone cores and reservoirs. Unlike pure brine case, the presence of oil shall influence the mobility of the CQDs. Figure 7a shows the BTCs of CQDs influenced by different values of residual oil saturation (S_{or}) in a sandstone core sample. As the oil saturation increases, the BTC shifts towards earlier breakthrough time as expected, bringing it forward from ~ 1PV at 0 % oil saturation to 0.67 PV at 44.6 %. However, the maximum breakthrough abilities show little difference and still can approach above 95 % after 3 PV's injection. The explanation for this could be that the transport of CQDs is confined in the aqueous phase due to their hydrophilic nature leading to an early breakthrough. By contrast, in the absence of an oil phase the CQDs have the entire pore volume to travel through during the entire injection process, leading to a delayed breakthrough, as illustrated by a schematic diagram in Figure 8.

To confirm this, CQD transport behaviour in a Berea sandstone core was simulated by using the modified 1-D advection-dispersion-reaction (ADR) equation with a modified porosity considering the effect of oil presence. The simulation method is described in section 2.3.2. The simulated lines in Figure 7a clearly show that there is a correspondence between the oil saturation and the position of breakthrough curves.

Based on the time (expressed in PV) when the CQDs breakthrough achieves 40%, 50% and 60%, the calibration curves (S_{or} against breakthrough time) are generated in Figure 7b. We plotted the residual oil saturation S_{or} (y axis) against the time points (x axis) cited from Figure 7a, when the simulated relative effluent concentration (C/C_0) approaches 40%, 50% and 60%. Good fittings (calibration curves) are achieved by using the logarithm fitting equation $y = \ln(b + ax)$.

Then the simulated calibration curves and a measured experimental breakthrough curve (as shown in Figure 7c) and are employed to determine the S_{or} in another sandstone core with a certain oil saturation (25.1%). The five-pointed star in Figure 7d shows that by using the best-fit calibration curve at 60% breakthrough, the calculated oil saturation is 24.0%.

4. CONCLUSIONS

It seems that the needs related to extracting practically-unscalable information from the subsurface hydrocarbon reservoir cannot be sufficiently met by currently intrusion or detection methods. Even the currently applied tracers are not enough to address this challenge, because most of these tracers, can only provide information about flow connectivity (i.e., the connection between where the tracer was injected and where it came out, without any information about its pathway in between) (Hwang et al. 2012). Derived from low-cost precursor, carbon quantum dots (CQDs) may provide a promising solution to locate and map the petroleum reservoir, due to its excellent migration ability in porous media, easy-detected luminescent property, and reservoir-friendly existence. Our results reveal that Xylose-CQDs had excellent stability against high ionic strength and high temperature, in terms of durable absorbance and fluorescent intensity, due to multi high-polarity functional group on their surface. Good consistence between the UV-Vis (on-line) and CLSM (off-line) confirms tracer-like migration capability in sandstone-packed column regardless of concentration and ionic

strength. Oil saturation detection was achieved by this CQDs based on its breakthrough properties influenced by the presence of oil phase.

Despite of its tracer-like breakthrough ability in the silica porous media, the transport capability of CQDs is heavily weakened in the calcite limestone rock which is positively charged. Therefore CQDs should be avoided used in the carbonate reservoir, or a comprehensive understanding of the underlying composition of the rock formation of the oil reservoir would be required in order to properly predict the behavior or such CQDs as well as to interpret the obtained fluorescence measures.

In terms of the environment impact and manufacturing cost, CQDs are still emerging particles that have a wealth of advantages for oil/gas applications. First, due to their intrinsic carbon-based components (Bhunia et al. 2013), there is no need to separate these particles from oil/gas products. CQDs are also biocompatible according to the cell viability tests (Gao et al. 2016b), which could minimize the contamination migrating from the environment to the biological chain. Despite of the energy-consuimging process of hydrothermal, the production cost of CQDs still has the possibltity to be low because of the cheap precursor of Xylose which is extremely abundant in nature wood.

Conflicts of interest

The authors declare no competing financial interests.

Acknowledgements

† Z. H. and H. G. had joint and equal contribution to senior authorship. This research has been funded by the European Research Council (ERC-2014-CoG, Project reference: 648375). Z. H.

was also receiving founding from University of Leeds and the China Scholarship Council (CSC) throughout his PhD.

Supporting information

The Supporting Information includes A core flooding setup and its schematic diagram for loading the real sandstone core; experiment condition of injecting CQDs into the sandstone core; Recorded evolution of time dependent transmission profiles of CQDs suspensions; Zeta potential and size distribution of CQDs in brine; The resolution of UV-Vis to measure the CQDs concentration. This material is available free of charge via the internet at http://pubs.acs.org.

REFERENCE

Alaskar, M., 2013. In-Situ Multifunctional Nanosensors for Fractured Reservoir Characterization. Department of Energy Resources Engineering. PhD. Stanford University, Stanford, California.

Bagaria, H.G., Xue, Z., Neilson, B.M., Worthen, A.J., Yoon, K.Y., Nayak, S., Cheng, V., Lee, J. H., Bielawski, C.W., Johnston, K.P., 2013. Iron oxide nanoparticles grafted with sulfonated copolymers are stable in concentrated brine at elevated temperatures and weakly adsorb on silica. ACS Appl. Mater. Interfaces 5, 3329-3339.

Becker, M.D., Wang, Y., Paulsen, J.L., Song, Y.Q., Abriola, L.M., Pennell K.D., 2015. In situ measurement and simulation of nano-magnetite mobility in porous media subject to transient salinity. Nanoscale 7, 1047-1057.

Berlin, J.M., Yu, J., Lu, W., Walsh, E.E., Zhang, L.L., Zhang, P., Chen, W., Kan, A.T., Wong, M.S., Tomson, M.B., Tour, J.M., 2011. Engineered nanoparticles for hydrocarbon detection in oil-field rocks. Energy Environ. Sci. 4, 505-509.

Bhunia, S.K., Saha, A., Maity, A.R., Ray, S.C., Jana, N.R., 2013. Carbon nanoparticle-based fluorescent bioimaging probes. Sci. Rep. 3, 1473.

Brusseau, M.L., Narter, M., Janousek, H., 2010. Interfacial partitioning tracer test measurements of organic-liquid/water interfacial areas: application to soils and the influence of surface roughness. Environ. Sci. Technol. 44, 7596-7600.

Dickens, G.R., Paull, C.K., Wallace, P., 1997. Direct measurement of in situ methane quantities in a large gas-hydrate reservoir. Nature 385, 426-428.

Ding, H., Yu, S.B., Wei, J.S., Xiong, H.M., 2016. Full-Color Light-Emitting Carbon Dots with a Surface-State-Controlled Luminescence Mechanism. ACS Nano 10, 484-491.

Gao, H., Sapelkin, A.V., Titirici, M.M., Sukhorukov, G.B., 2016a. In Situ Synthesis of Fluorescent Carbon Dots/Polyelectrolyte Nanocomposite Microcapsules with Reduced Permeability and Ultrasound Sensitivity. ACS Nano 10, 9608−9615.

Gao, H., Wen, D., Tarakina, N.V., Liang, J., Bushby, A.J., Sukhorukov, G.B., 2016b. Bifunctional ultraviolet/ultrasound responsive composite TiO2/polyelectrolyte microcapsules. Nanoscale 8, 5170-5180.

Gao, H., Wen, D., Sukhorukov, G.B., 2015. Composite silica nanoparticle/polyelectrolyte microcapsules with reduced permeability and enhanced ultrasound sensitivity. J. Mater. Chem. B 3, 1888-1897.

Hu, Z., Azmi, S.M., Raza, G., Glover, P.W.J., Wen, D., 2016. Nanoparticle-Assisted Water-Flooding in Berea Sandstones. Energy Fuel 30, 2791-2804.

Hu, Z., Nourafkan, E., Gao, H., Wen, D., 2017. Microemulsions stabilized by in-situ synthesized nanoparticles for enhanced oil recovery. Fuel 210, 272-281.

Huh, C., Bryant, S.L., Milner, T.E., Johnston, K.P., 2015. Determination of oil saturation in reservoir rock using paramagnetic nanoparticles and magnetic field. US Patent 9133709B2.

Hwang, C.C., Ruan, G., Wang, L., Zheng, H., Samuel, E.L., Xiang, C., Lu, W., Kasper, W., Huang, K., Peng, Z., Schaefer, Z., Kan, A.T., Marti, A.A., Wong, M.S., Tomson, M.B., Tour, J.M., 2014. Carbon-based nanoreporters designed for subsurface hydrogen sulfide detection. ACS Appl. Mater. Interfaces 6, 7652-7658.

Hwang, C.C., Wang, L., Lu, W., Ruan, G.D., Kini, G.C., Xiang, C.S., Samuel, E.L.G., Shi, W., Kan, A.T., Wong, M.S., Tomson, M.B., Tour, J.M., 2012. Highly stable carbon nanoparticles designed for downhole hydrocarbon detection. Energy Environ. Sci. 5, 8304-8309.

Jones, E.H., Smith, C.C., 2005. Non-equilibrium partitioning tracer transport in porous media: 2-D physical modelling and imaging using a partitioning fluorescent dye. Water Res. 39, 5099-5111.

Kini, G.C., Yu, J., Wang, L., Kan, A.T., Biswal, S.L., Tour, J.M., Tomson, M.B., Wong, M.S., 2014. Salt- and temperature-stable quantum dot nanoparticles for porous media flow. Colloids Surf. A 443, 492-500.

Kondiparty, K., Nikolov, A., Wu, S., Wasan, D., 2011. Wetting and spreading of nanofluids on solid surfaces driven by the structural disjoining pressure: statics analysis and experiments. Langmuir 27, 3324-3335.

Luo, D., Wang, F., Zhu, J., Cao, F., Liu, Y., Li, X., Willson, R.C., Yang, Z., Chu, C.W., Ren, Z., 2016. Nanofluid of graphene-based amphiphilic Janus nanosheets for tertiary or enhanced oil recovery: High performance at low concentration. Proc. Natl. Acad. Sci. U.S.A. 113, 7711-7716.

Sabir, I.H., Haldorsen, S., Torgensen, J., Alestrom, P., Gaut, S., Colleuille, H., Pedersen, T.S. and Kitterod, N.O., 2000. Synthetic DNA tracers: examples of their application in water related studies. Tracers and Modelling in Hydrogeology 262, 159-165.

Skaug, M.J., Wang, L., Ding, Y., Schwartz, D.K., 2015. Hindered nanoparticle diffusion and void accessibility in a three-dimensional porous medium. ACS Nano 9, 2148-2156.

Stuart, M.A., Huck, W.T., Genzer, J., Muller, M., Ober, C., Stamm, M., Sukhorukov, G.B., Szleifer, I., Tsukruk, V.V., Urban, M., Winnik, F., Zauscher, S., Luzinov, I., Minko, S., 2010. Emerging applications of stimuli-responsive polymer materials. Nat. Mater. 9, 101-113.

Tang, G., Mayes, M.A., Parker, J.C., Jardine, P.M., 2010. CXTFIT/Excel–A modular adaptable code for parameter estimation, sensitivity analysis and uncertainty analysis for laboratory or field tracer experiments. Comput. Geosci. 36, 1200-1209.

Wang, C., Bobba, A.D., Attinti, R., Shen, C., Lazouskaya, V., Wang, L.P., Jin, Y., 2012. Retention and transport of silica nanoparticles in saturated porous media: effect of concentration and particle size. Environ. Sci. Technol. 46, 7151-7158.

Wang, Y., Li, Y., Fortner, J.D., Hughes, J.B., Abriola, L.M., Pennell, K.D., 2008. Transport and retention of nanoscale C60 aggregates in water-saturated porous media. Environ. Sci. Technol. 42, 3588-3594.

Wang, Y., Becker, M.D., Colvin, V.L., Abriola, L.M., Pennell, K.D., 2014. Influence of Residual Polymer on Nanoparticle Deposition in Porous Media. Environ. Sci. Technol. 48, 10664-10671.

Wasan, D.T., Nikolov, A.D., 2003. Spreading of nanofluids on solids. Nature 423, 156-159.

Yang, X., Zhuo, Y., Zhu, S., Luo, Y., Feng, Y., Dou, Y., 2014. Novel and green synthesis of high-fluorescent carbon dots originated from honey for sensing and imaging. Biosens. Bioelectron. 60, 292-298.

Yu, H., 2012. Transport and retention of surface-modified nanoparticles in sedimentary rocks. Department of Petroleum and Geosystems Engineering. PhD. The University of Texas at Austin, Austin, Texas. http://hdl.handle.net/2152/22237.

Yu, H., He, Y., Li, P., Li, S., Zhang, T., Rodriguez-Pin, E., Du, S., Wang, C., Cheng, S., Bielawski, C. W., Bryant, S. L., Huh, C., 2015. Flow enhancement of water-based nanoparticle dispersion through microscale sedimentary rocks. Sci. Rep. 5, 8702.

Table 1. Experimental conditions of CDs transport studies conducted in brine-saturated glass column packed with either 30-40 mesh glass beads (G) or limestone (LS)

Exp.	v_p^a (m/d)	V_P^b (ml)	$\emptyset^c$(%)	C_0^d (ppm)	PW^e (PV)	IS^f(mM CaCl2 or API)	Temperature (^{o}C)	MB^f (%)
G1	2.56	12.8±0.18	38.02	10.61	3.0	1	25	98.75
G2	2.56	12.8±0.18	38.02	24.78	3.0	1	25	102.5
G3	2.56	12.8±0.18	38.02	8.77	3.0	10	25	96.85
G4	2.56	12.8±0.18	38.02	9.64	3.0	100	25	97.5
G5	2.56	12.8±0.18	38.02	8.89	3.0	200	25	96.06
G6	2.56	12.8±0.18	38.02	12.05	3.0	API	25	100
G7	2.56	12.8±0.18	38.02	9.86	3.0	API	60	98.75
G8	2.56	12.8±0.18	38.02	10.06	3.0	API	80	98.75
L1	2.56	12.8±0.18	38.02	10.36	3.0	API	25	98.75

[a] Pore water velocity; [b] Pore volume; [c] Porosity; [d] influent concentration; [e] volume of fluids injected; [f] ionic strength; [f] mass balance of nanoparticle.

Table 2. Mass balance for CQDs transport experiments conducted in brine-saturated glass column packed with either 30-40 mesh glass beads (GB) or limestone (LS)

Exp.	Influent Conc. (ppm)	Substrate	pH	Total CDs injected (µg)	CDs out after injection (µg)	CDs left in column after injection (µg)	Error,%	CDs out in Post-flushing (µg)	CDs left in column after Post-flushing (µg)	Retained percentage after post-flushing, (%)
G1	10.61	GB	6.5	424.5	256.2	163.0	1.25	151.0	11.8	2.8
G2	24.78	GB	6.7	992.1	638.7	378.1	-2.5	352.5	25.6	2.6
G3	8.77	GB	6.5	350.7	201.4	138.3	3.15	125.7	12.6	3.6
G4	9.64	GB	6.9	385.5	230.4	145.4	2.5	145.2	0.26	0.1
G5	8.89	GB	7.2	355.7	203.0	138.7	3.94	125.7	13.1	3.7
G6	12.05	GB	7.4	391.5	222.3	169.2	0	167.2	1.97	0.5
G7	9.86	GB	6.9	394.3	196.6	192.8	1.25	171.4	21.4	5.5
G8	10.06	GB	7.1	386.3	152.6	228.9	1.25	201.1	27.8	7.3
L1	10.36	Calcium	6.8	414.4	124.8	284.4	1.25	127.8	156.6	37.8

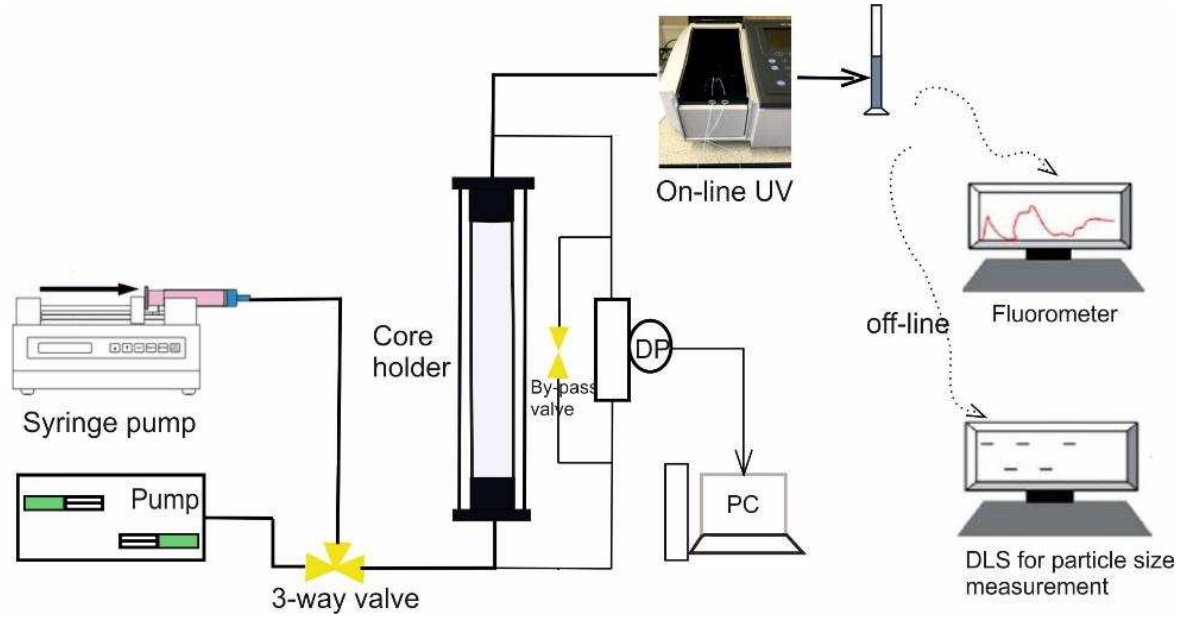

Figure 1. Schematic of the apparatus for laboratory detection and quantitative analysis of CQDs in simulated reservoir rock. The concentration of particles was detected on-line by UV-Vis spectrophotometer, running at a wavelength of 310 nm.

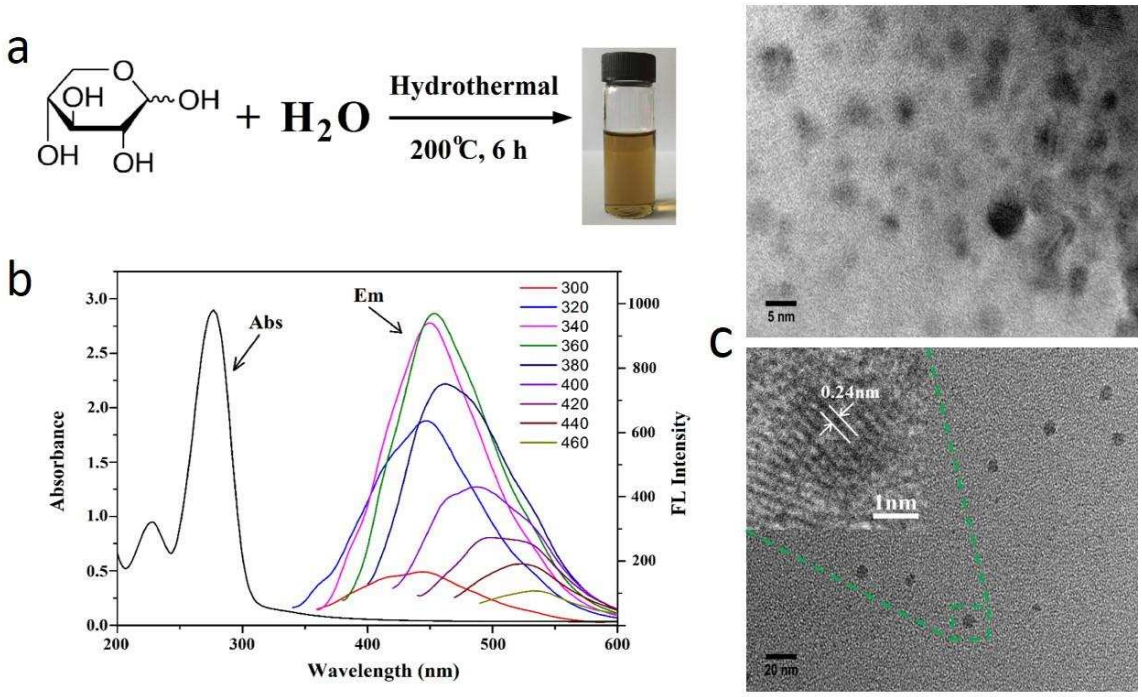

Figure 2. Synthesis and characterization of CQDs. a) Schematic diagram of one-pot synthesis of carbon quantum dots (CQDs) from xylose. b) UV-Vis absorbance and fluorescence emission spectra of the obtained CQDs. c) TEM images (up and down), and high-resolution TEM images (inset in the downside) for CQDs with identical lattice fringes.

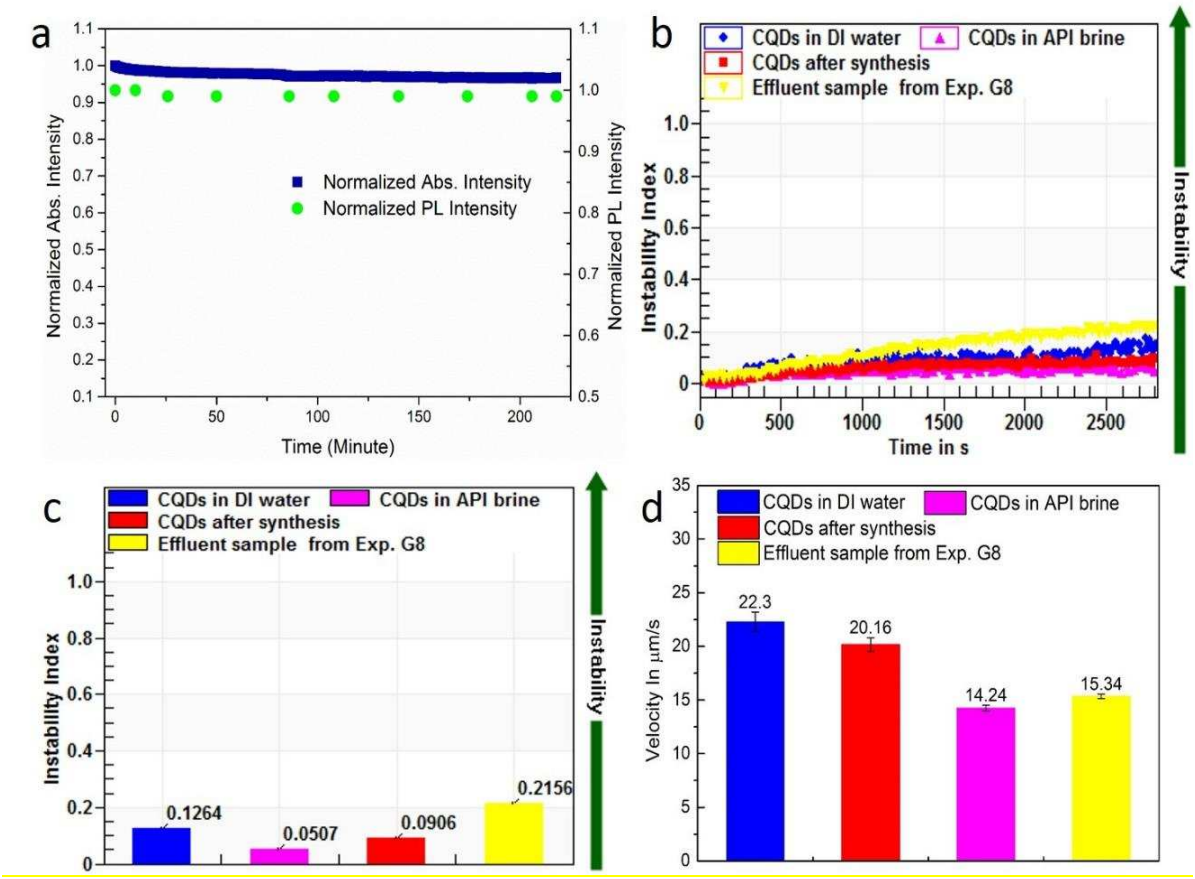

Figure 3. Stability of four CQDs samples. a) Absorbance at a fixed light wavelength of 278 nm and fluorescence intensity under excitation of 360 nm UV light for CQD dispersed in API brine, for a period up to 220 min; b) Instability index; c) Cumulative instability index. Higher index means less stability; d) Sedimentation velocity analysed by front tracking method.

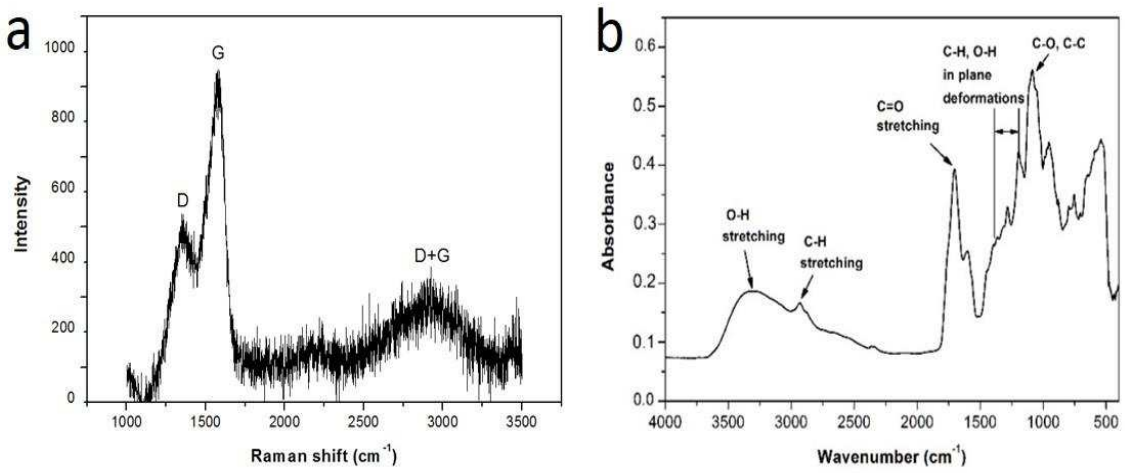

Figure 4. Surface analysis of CQDs. a) Raman spectra. b) FTIR spectra of the CQDs.

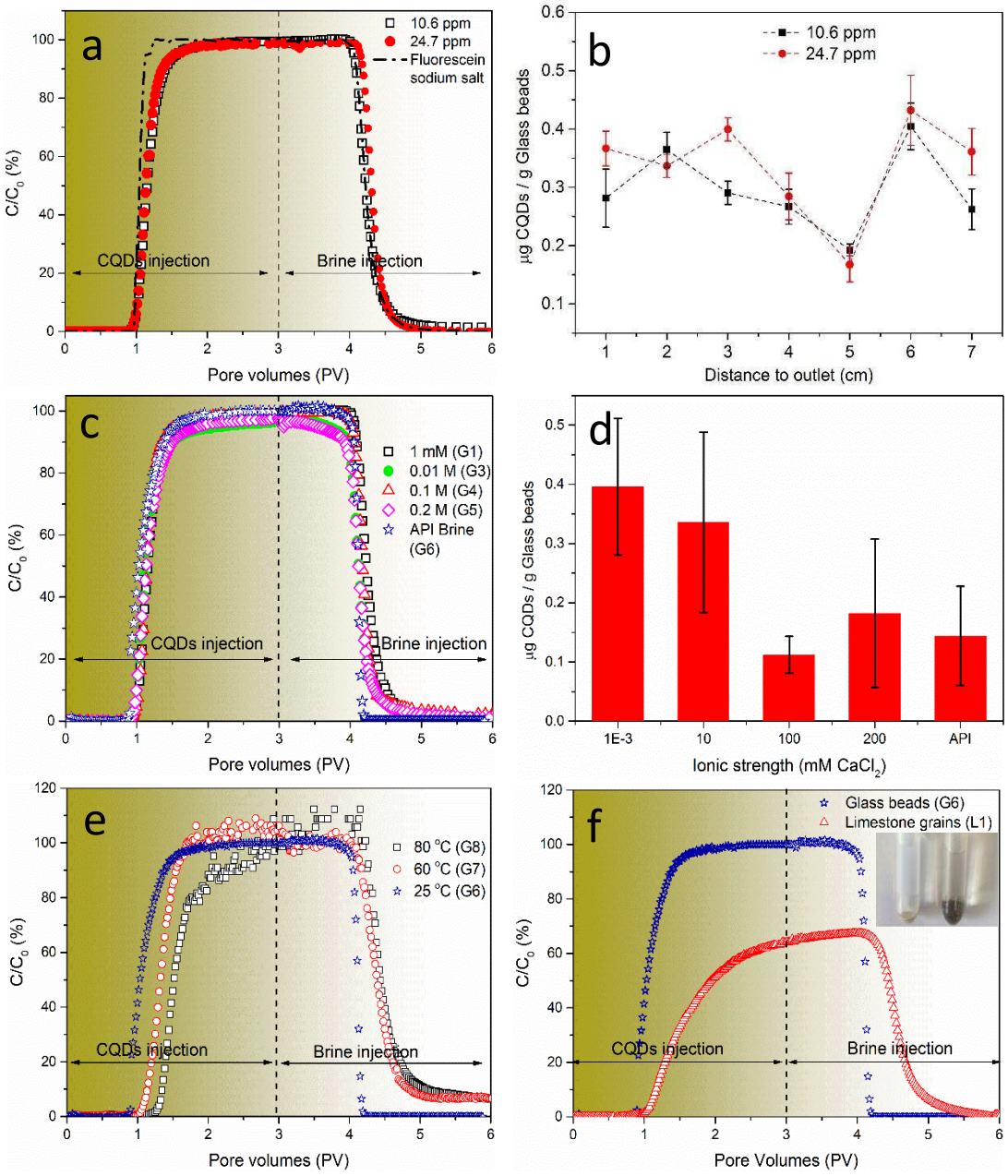

Figure 5. Transport properties of CQDs in columns packed with glass beads and calcite grains. a) BTCs for CQD suspension at two concentrations (10.6 ppm and 24.7 ppm) and BTC for a typical tracer (fluorescein sodium salt). b) Retention profiles for CQDs at different positions in the column (the dashed line is just for guiding the eye). c) BTCs for CQDs (~10 ppm) in columns of glass bead packs, at room temperature, with varying ionic strengths of the base electrolyte (from 1 mM $CaCl_2$ to standard of API brine). The experiment conditions have been listed in Table 1. d) CQDs retention in the columns at various suspension salinities, based on

mass balance. e) BTCs for CQDs dispersed in API brine, and in glass bead column at elevated temperatures (25, 60 and 80 ^{o}C). f) BTCs for CQDs transport in glass bead and calcite column. The inset is optical image of (1) original calcite rock grains, and (2) those extracted from the column of calcite pack after the experiment and having been washed with API brine four times.

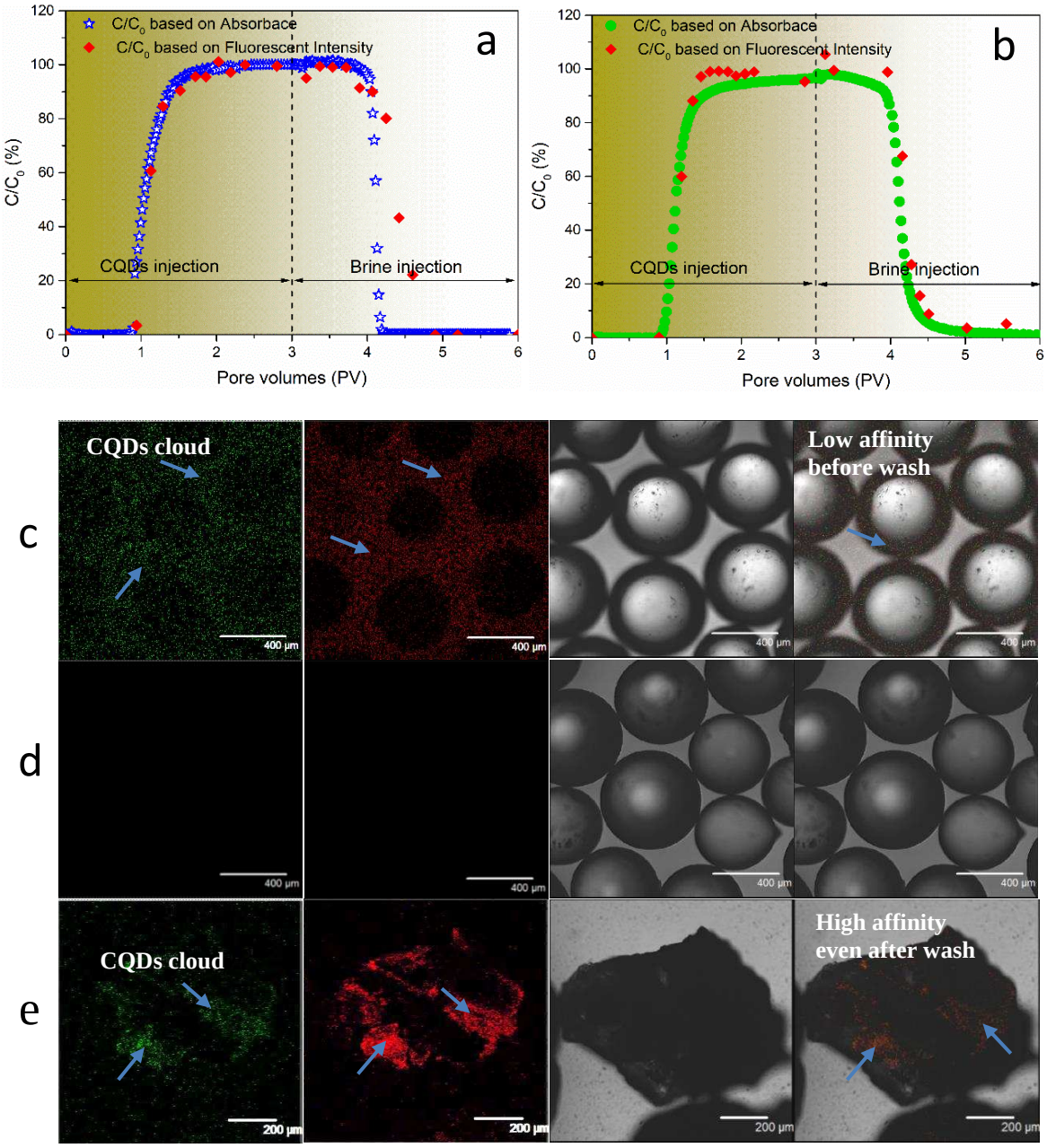

Figure 6. Coupled absorbance and fluorescence methods to determine the CQD concentration for the transport experiments. a) Break through curves (BTCs) for exp. G6, in Table 1, measured with both in-line UV-Vis spectrophotometer and Off-line fluorescence spectroscopy, using API brine as the process solution. b) BTCs determined in the same manner as in Figure 6a but for exp. G3 using 10 mM $CaCl_2$ (Table 1). c) CLSM images of glass beads extracted from the column in exp. G6. The images from left to right are: fluorescent images of CQDs irradiated by laser at 488 nm and re-emitting green light, fluorescent images irradiated by laser

at 561 nm and re-emitting red light, optical image of glass beads, and overlap images of the CQDs and the optical glass beads image. d) CLSM images of glass beads extracted from column after exp. G6 and washed with particle-free API brine. Images in the same order as in Figure 6c. e) CLSM images of calcite rock pieces extracted from the column after exp. L1 and washing with API brine.

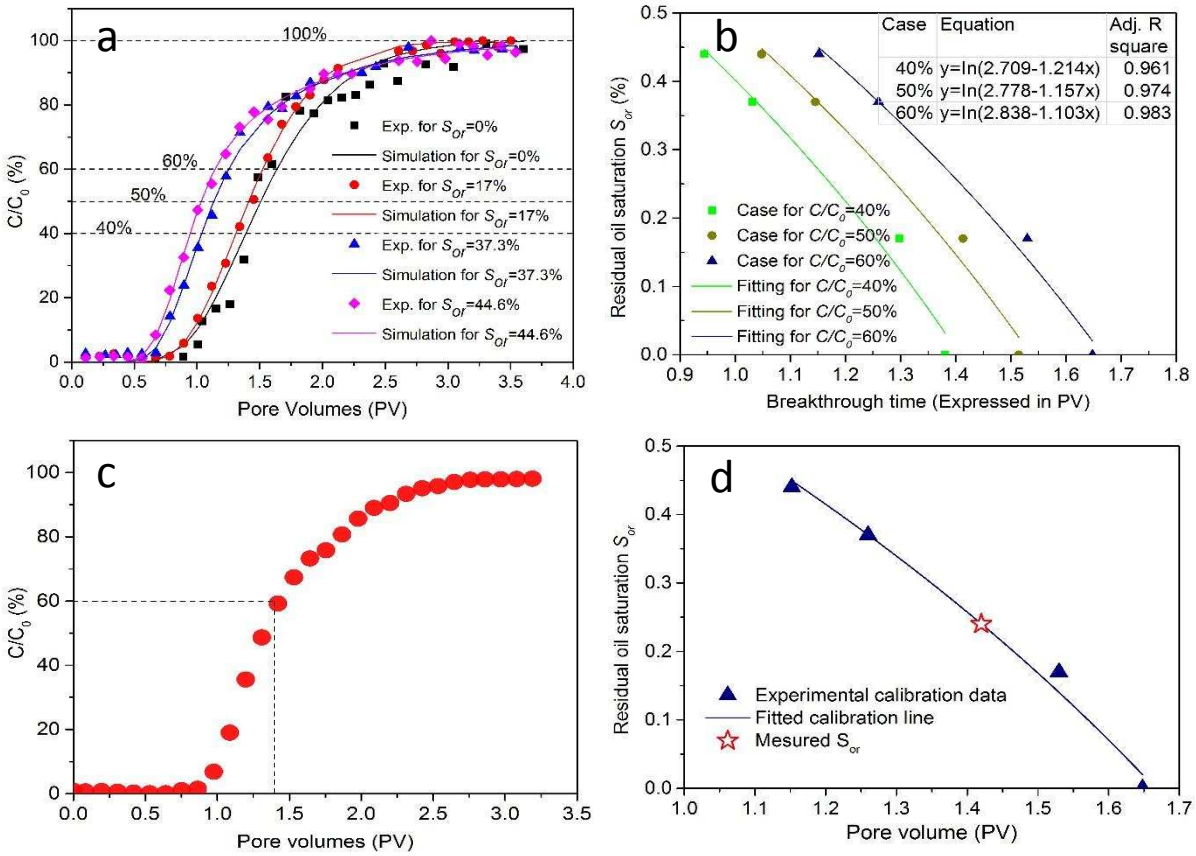

Figure 7. Using CQDs to detect the fractional residual oil saturation in a sandstone core. a) Breakthrough curves a function of injection time for samples containing different water fractions at S_{or}, when injecting CQD suspension at 0.5 mL/min into sandstone core. b) Residual oil saturation as a function of the volume of throughput required for the relative effluent CQD concentration (C/C_0) to reach 40%, 50% and 60%, together with appropriate fitted curves of the form $y = \ln(b + ax)$. c) The experimental breakthrough profile in sandstone with the pre-set residual oil saturation (S_{or}) of 25.1 %. d) Find the breakthrough time (PV) at 60% of C/C_0 in Figure 7c, then from breakthrough time to calculate the oil saturation using the calibration curve (the blue line in Figure 7b).

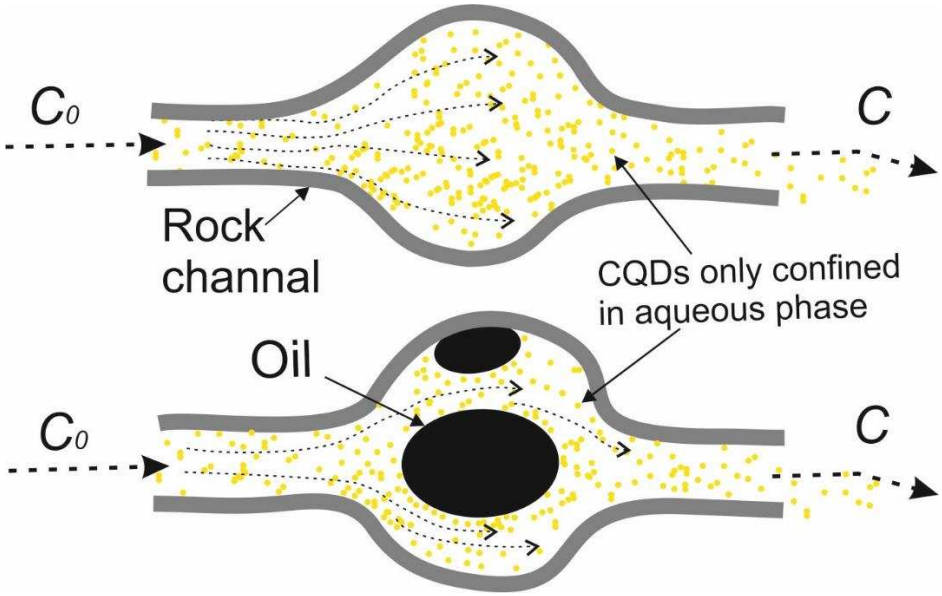

Figure 8. Microscale schematic diagram of CQDs transport affected by the presence of oil.